batteries

MDPI

Article

Investigation on the Air Stability of P2-Layered Transition Metal Oxides by Nb Doping in Sodium Ion Batteries

Yanyan Chen [1,2,†], Qinhao Shi [2,†], Shengyu Zhao [2], Wuliang Feng [2,*], Yang Liu [2], Xinxin Yang [2], Zhenwei Wang [1,*] and Yufeng Zhao [2,*]

[1] School of Chemical and Environmental Engineering, Shanghai Institute of Technology, Shanghai 201418, China
[2] Institute for Sustainable Energy & College of Sciences, Shanghai University, Shanghai 200444, China
* Correspondence: wuliangfeng@shu.edu.cn (W.F.); wangzhenwei@sit.edu.cn (Z.W.); yufengzhao@shu.edu.cn (Y.Z.)
† These authors contributed equally to this work.

Abstract: Sodium-ion batteries are regarded as a substitution for lithium-ion batteries for its abundant resources, wide distribution, low cost, etc. The P2-layered sodium transition metal oxides (P2-Na_xTMO_2) have attracted extensive attention due to their high rate and cycling properties. However, P2-Na_xTMO_2 often undergoes structural transformations when exposed in ambient air, which restricts its practical applications. Herein we studied the effect of Nb doping on the air stability of P2-Na_xTMO_2. We demonstrated that the Nb-induced surface preconstructed layer inhibited the surface dissolution of the P2 material in the electrochemical reaction and formed a stable and thin (cathode–electrolyte interphase) CEI film, which prevented water molecules from entering the P2-Na_xTMO_2 lattice. $Na_{0.67}Mn_{0.67}Ni_{0.33}Nb_{0.03}O_2$ could exhibit superior rate performance (a reversible capacity of 72.5 mAh g^{-1} at 20 C) and outstanding cycling performance (84.43% capacity retention after 1000 cycles at 5 C) in a half cell after exposed in a moisture atmosphere (RH93%) for 20 days.

Keywords: sodium-ion batteries; P2-layered sodium transition metal oxides; air stability; surface preconstructed layer

Citation: Chen, Y.; Shi, Q.; Zhao, S.; Feng, W.; Liu, Y.; Yang, X.; Wang, Z.; Zhao, Y. Investigation on the Air Stability of P2-Layered Transition Metal Oxides by Nb Doping in Sodium Ion Batteries. *Batteries* **2023**, *9*, 183. https://doi.org/10.3390/batteries9030183

Academic Editors: Yu Jiang and Stefan Adams

Received: 17 December 2022
Revised: 4 March 2023
Accepted: 11 March 2023
Published: 20 March 2023

1. Introduction

Lithium-ion batteries (LIBs) are known for their high energy density but they are not suitable for large-scale energy storage due to the limitation of lithium reserves [1–3]. Therefore, new energy storage systems with lower costs should be developed to support lithium's sustainable development [4–6]. In recent years, the sodium-ion battery has attracted wide attention because of its abundant sodium resources, low cost, good comprehensive performance, and the same working principle and similar battery components as the lithium-ion battery [7–11]. Sodium-ion batteries meet the requirements of low cost, long life, and high safety in the field of sustainable energy, and to some extent ease the limitation of the shortage of lithium resources on the development of energy storage batteries [9,12]. Since the late 1970s, when researchers found that Na^+ can be reversibly dragged/embedded in the layered oxide Na_xCoO_2, more and more studies have been conducted on the cathode materials of sodium-ion batteries [13,14]. The cathodes mainly include the layered oxide, polyanion, Prussian blue and organics [15–18]. The layered oxide material is the main cathode material of the sodium-ion battery because of its advantages of simple production, high specific capacity and high operating voltage [19–23].

Layered oxides are the earliest kind of embedded compounds studied and the general formula of the structure is Na_xTMO_2 (TM is mainly one or more transition metal elements). Usually, the transition metal elements and the MO_6 polyhedron structure formed by the surrounding six oxygen atoms form the transition metal layer, and the sodium ion is located

between the transition metal layer, forming the layered structure of the MO_6 polyhedron layer and the NaO_6 alkali metal layer arranged alternately. Delmas et al. divided layered oxides into O3, O2, P3 and P2 according to the coordination configuration of the sodium ion and the stacking mode of oxygen in MO_6 polyhedron [24]. The P2 and O3 phases stand for the prismatic and octahedral coordination configuration of the sodium ion, with ABBA or ABCABC stacking, respectively; the number represents the number of stacks with minimum oxygen repetition units [25]. Nowadays, most of the research on Na_xTMO_2 has focused on improving electrochemical performance, such as achieving high energy density and long cycle life [26,27]. However, Na_xTMO_2 are hygroscopic and unstable in ambient air, which limits their practical application [28–33]. The hygroscopic and air instability of $NaxTMO_2$ results in increased costs and hinders their commercialization. Therefore, it is of practical significance to study the air stability of cathode materials [34–36].

Studies have shown that $NaMn_{0.5}Ni_{0.5}O_2$ (mixed with an electronic conductor and binder) slurry made in ambient air usually show obvious particle agglomeration [37]. Due to the strong alkalescence of $NaMn_{0.5}Ni_{0.5}O_2$ particles, OH^- reacts with polyvinylidene fluoride (PVDF) in the slurry, resulting in the removal of F from PVDF and poor bonding performance. By means of thermogravimetric analysis, gas generation analysis and neutron pair distribution function, Nazar et al. found that P2-$Na_{0.67}Fe_{0.5}Mn_{0.5}O_2$ instability in humid air was caused by the reaction of water and carbon dioxide to generate CO_3^{2-}, which would enter the tetrahedral gap of the transition metal layer [19]. At the same time, Mn^{3+} would change into Mn^{4+} to maintain charge balance. Compared with $Na_{0.67}Fe_{0.5}Mn_{0.5}O_2$ with surface protection, the water contaminated $Na_{0.67}Fe_{0.5}Mn_{0.5}O_2$ showed more serious polarization and lower specific capacity. Yang Yong et al. found that there was a critical sodium content (denoted by n_c) in P2-type layered oxide cathode materials, through a series of comparative experimental studies and theoretical calculations [38]. When the sodium content was higher than n_c, water molecules could not embed in the material. However, the reasons for the structural transformation of materials in wet environments, especially the mechanism by which water molecules were inserted into the sodium layer and which factors dominated the structural transformation, have not been further investigated [39–45].

In this work, based on the P2-$Na_{0.67}Mn_{0.67}Ni_{0.33}O_2$ (P2-$Na_{0.67}$MN) and P2-$Na_{0.67}Ni_{0.33}Mn_{0.67}Nb_{0.03}O_2$ (P2-$Na_{0.67}$MNNb), we explored the effect of Nb doping on air and electrochemical stabilities. Nb doping increased the c-axis spacing of P2-$Na_{0.67}$MN, introduced a strong Nb-O bond (753 kJ mol^{-1}), induced the formation of a preconstructed layer on the surface, and greatly improved the air stability and electrochemical stability. Characterizations such as XRD, SEM and TEM were applied to reveal the behavior and structural transformation mechanism of P2-$Na_{0.67}$MN before and after Nb doping in different environments.

2. Experimental Section

2.1. Synthesis of Materials

The raw materials were purchased from Sigma-Aldrich (Saint Louis, MO, USA). The following acetate salts were used in the synthesis of the target products [$Mn(CH_3COO)_2 \cdot 4H_2O$, $Ni(CH_3COO)_2 \cdot 4H_2O$, Alfa Aesar (Haverhill, MA, USA)]. The method used for the synthesis of the target products was co-precipitation. Firstly, 0.036 mol manganese acetate and 0.018 mol nickel acetate were accurately weighed. Then, 50 mL deionized water was added to dissolve the mixture, and the mixture was stirred with mechanical agitator for 60 min. Next, we dissolved 0.07 mol Na_2CO_3 with 20 mL deionized water. The sodium carbonate solution was transferred to the transition metal solution at a rate of 2 mL min^{-1} using a micro-peristaltic pump. After a reaction of 18 h, this solution was washed three times in deionized water and in ethanol and put in a vacuum drying oven at 80 °C for 10 h. The SEM images of the precursor after drying are shown in Figure S1. The 0.8 g precursor was fully ground with sodium carbonate according to the specific molar ratio. At this time, niobium pentoxide with a theoretical molar ratio of 0.03 was added; adding

excessive niobium pentoxide produced impurity peaks (Figure S2). The ground powder was put into a muffle furnace for sintering at 500 °C, 10 h and 900 °C, 10 h.

2.2. Humid Environment Setting

Three different environments were set ((1) RH93% humid environment, (2) RH75% humid environment and (3) conventional atmosphere, labeled Air in the picture). Specific operations regarding wet conditions will be explained in detail. The saturated salt solution of $NaHCO_3$ was first prepared and the target product was placed in the centrifuge tube, followed by the saturated salt solution of sodium carbonate and the target product in a closed box. Then, we placed the enclosed box in an oven set at 40 °C. The hygrometer accurately measured RH93%. Repeating the above steps, saturated sodium chloride solution produced a stable humidity of 75% (as measured using a hygrometer) at a closed chamber of 40 °C. According to the experimental requirements, the target product was placed for a fixed number of days to obtain the experimental results.

2.3. Material Characterization

The crystal structure of the cathode material was determined using X-ray powder diffraction (Smartlab 9 kw, Rigaku, Tokyo, Japan). The FullProf software (FullProf Suite Linux (64 bits)) was used for Rietveld refinement. The morphology of the cathode materials was characterized using scanning electron microscopy (SEM, ZEISS sigma300, Oberkochen, Germany). The microstructure of the material was characterized using TEM JEOL 2100F (Tokyo, Japan) and energy dispersive spectroscopy (EDS). The chemical composition of the material was acquired by inductively coupled plasma-atomic emission spectrometry (ICP-AES, PERKINE 7300DV, Perkin Elmer, Waltham, MA, USA). Fourier infrared spectroscopy (Nexus 670, Thermo Nicolet, USA) was used to obtain information about chemical bonds.

2.4. Electrochemical Measurement

The active material, Super P, and binder PVDF were mixed in a mass ratio of 8:1:1. The ground powder was dissolved with N-methyl-2-pyrrolidone (NMP) solvent and put into a small bottle for stirring [46]. The electrode was dried in a vacuum oven for drying at 80 °C for 10 h and was cut in pieces with a diameter of 12 mm. An amount of 1 M $NaClO_4$ in EC: PC (1:1 + 5% FEC) was used as the electrolyte. The electrodes were assembled into a coin cell (CR2032) in a glovebox filled with argon gas using Whatman fiberglass as a separator. The LAND CT2001A test system was used to test the charge–discharge performance under different currents. Electrochemical impedance (EIS) was measured using the CHI660 electrochemical workstation.

3. Results and Discussion

P2-$Na_{0.67}$MNNb and P2-$Na_{0.67}$MN were prepared using a simple co-precipitation method. The specific element compositions of P2-$Na_{0.67}$MNNb and P2-$Na_{0.67}$MN were obtained using inductively coupled plasma-atomic emission spectrometry (Table S1), which was in line with the design experiment expectations. The crystal structure of the target sample was identified using X-ray powder diffraction (XRD) and Rietveld refinement, as shown in Figure 1a,b. All the diffraction peaks were well matched, indicating that the target product was successfully prepared with high crystallinity. All the peaks of P2-$Na_{0.67}$MNNb and P2-$Na_{0.67}$MN belonged to a hexagonal system with a space group of $P6_3/mmc$ (space group no. 194) [35]. The crystallographic parameters of P2-$Na_{0.67}$MNNb and P2-$Na_{0.67}$MN are shown in Tables S2 and S3. As shown in Figure 1c, the refined crystal structure showed that Nb doping expanded the c-axis parameter from 1.1155 to 1.1161 nm and expanded the a-axis parameter from 0.2885 to 0.2887 nm. After Nb doping, the parameters of c-axis and a-axis of P2-$Na_{0.67}$MNNb increased. The refined structure of P2-$Na_{0.67}$MNNb showed that Nb ions occupied the Ni site in the octahedral layers. The transition metals Mn, Ni and Nb in P2-$Na_{0.67}$MNNb constituted the transition metal layer (represented by the blue parallelogram), and sodium ions (represented by the yellow spheres) were located between

the transition metal layers, forming a layered structure with an alternating polyhedron layer and alkali metal layer.

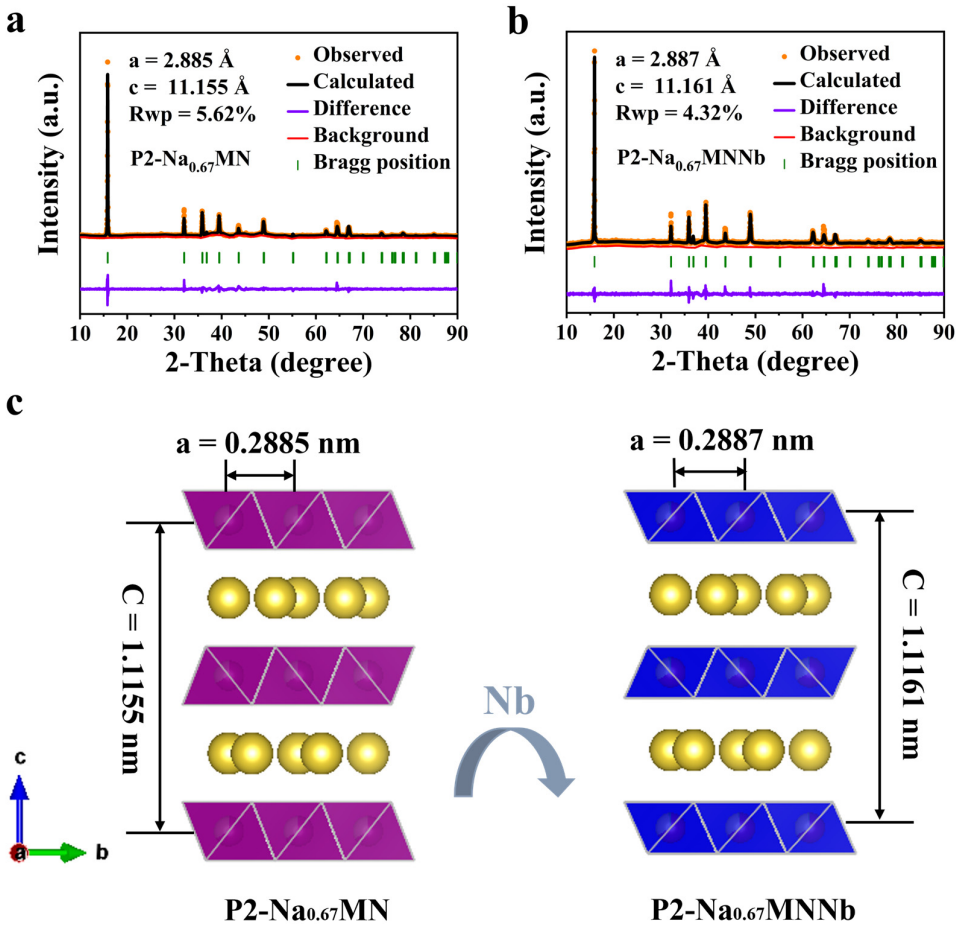

Figure 1. Rietveld refinement plots of (**a**) P2-$Na_{0.67}$MN and (**b**) P2-$Na_{0.67}$MNNb. (**c**) The crystal structures of P2-$Na_{0.67}$MN and P2-$Na_{0.67}$MNNb.

To explore the influence of Nb doping on P2-Na_xTMO_2 material, we took P2-$Na_{0.67}$MN and P2-$Na_{0.67}$MNNb as examples. Three environments were set: (1) ambient air, (2) RH75% humid environment and (3) RH93% humid environment (the setting methods of the three environments were referred to in Section 2). As shown in the Figure 2a,b, the XRD patterns of P2-$Na_{0.67}$MN and P2-$Na_{0.67}$MNNb did not change significantly in the three environments after a day of exposure, which indicated that one day did not lead to severe hydration. When exposure time was further extended to 8 days, hydration peaks of 12.6° and 25.5° were obviously observed in P2-$Na_{0.67}$MN (RH93% humid environment, Figure 2c). However, the XRD pattern of P2-$Na_{0.67}$MN remained unchanged in relatively dry air, which indicated that water was one of the necessary factors for P2-Na_xTMO_2 instability. Compared with the phenomenon of hydration peaks generated from P2-$Na_{0.67}$MN in a humid environment, the XRD pattern of P2-$Na_{0.67}$MNNb material remained unchanged and the position of the peak fitted well with the initial position, indicating that the air stability of P2-$Na_{0.67}$MNNb was better than P2-$Na_{0.67}$MN (Figure 2d). The results showed that P2-$Na_{0.67}$MNNb was more stable than P2-$Na_{0.67}$MN in a humid environment. The doping of Nb element effectively improved the air stability of P2-$Na_{0.67}$MN material.

To further investigate the air stability of P2-$Na_{0.67}$MNNb, P2-$Na_{0.67}$MNNb was exposed to air and RH93% humid environment for 20 days, respectively. The XRD pattern shows (Figure S3a) that the peak position was not shifted and no hydration peak was formed. The doping of Nb element effectively improved the air stability of P2-$Na_{0.67}$MN. Figure S3b shows the XRD patterns of P2-$Na_{0.67}$MNNb powder soaked in water for 0.5 h and 14 h. No obvious changes were observed, indicating that this sample exhibited a strong

shielding effect on water and outstanding air stability, which was consistent with the above statement. The bonding energy of Nb-O (753 kJ mol^{-1}) > Mn-O (402 kJ mol^{-1}) > Ni-O (391 kJ mol^{-1}) indicated that the doping of Nb introduced the strong bond energy of Nb-O, which not only improved the stability of the transition metal layer but also improved the air stability.

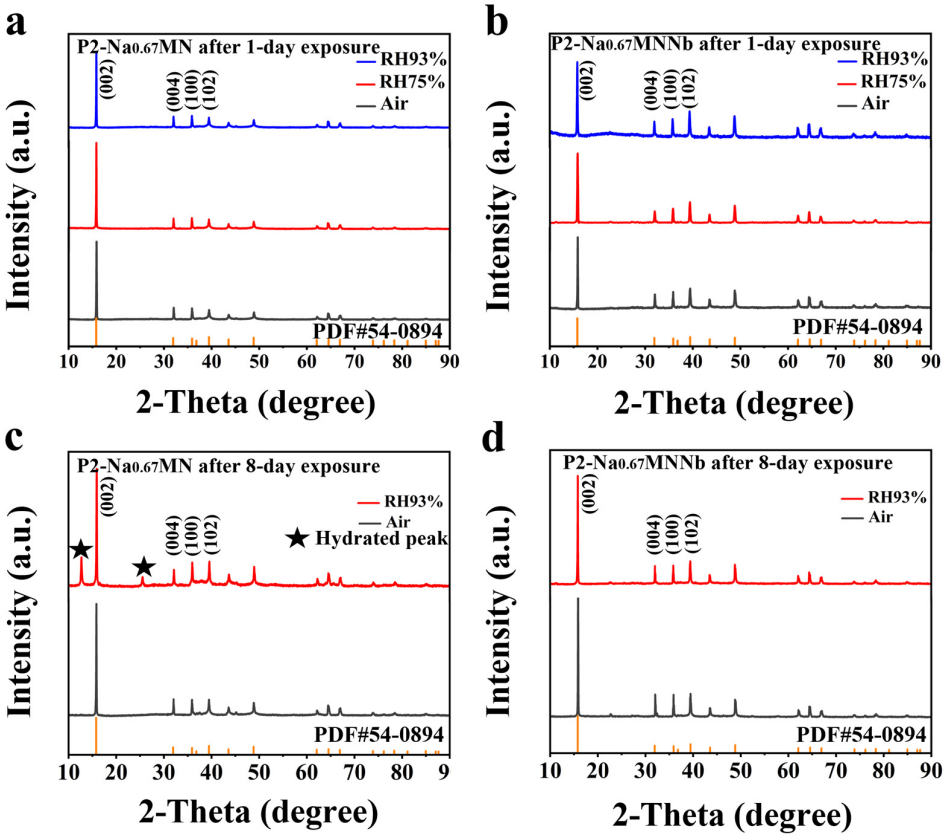

Figure 2. The XRD patterns of (**a**) P2-$Na_{0.67}$MN and (**b**) P2-$Na_{0.67}$MNNb samples exposed in different atmospheres after 1 day of exposure. The XRD patterns of (**c**) P2-$Na_{0.67}$MN and (**d**) P2-$Na_{0.67}$MNNb samples exposed in different atmospheres after 8 days of exposure.

To further investigate the process of P2-Na_xTMO_2 undergoing air exposure, the morphological characteristics and particle size of the target material were studied using emission scanning electron microscopy (Figure 3a–i). Figure 3a,d,g shows the unexposed morphologies of P2-$Na_{0.67}$MN and P2-$Na_{0.67}$MNNb. P2-$Na_{0.67}$MN was composed of regular sheet particles. The bulk particles were about 1.9 µm in diameter. P2-$Na_{0.67}$MNNb consisted of regular particles, each of which had a standard hexagonal edge and a smooth surface, with a diameter of about 1.05 µm. The results showed that the morphology and particle size of P2-$Na_{0.67}$MN are significantly improved by the effective doping of niobium [47]. As shown in Figure 3b, P2-$Na_{0.67}$MN was placed in a humid environment with RH93% for 8 days, and the SEM images showed the formation of impurities on its surface. Meanwhile, the surface of P2-$Na_{0.67}$MNNb remained smooth (Figure 3e,h). After being placed in a humid environment with RH93% for 20 days, SEM images showed that impurities were still generated on the surface of P2-$Na_{0.67}$MN (Figure 3c). However, the surface of P2-$Na_{0.67}$MNNb remained smooth, which was consistent with XRD results (Figure 3f,i). These impurities were the result of water molecule insertion into the sample P2-$Na_{0.67}$MN, which was sufficient to indicate that P2-$Na_{0.67}$MN has a weaker defense against water than P2-$Na_{0.67}$MNNb.

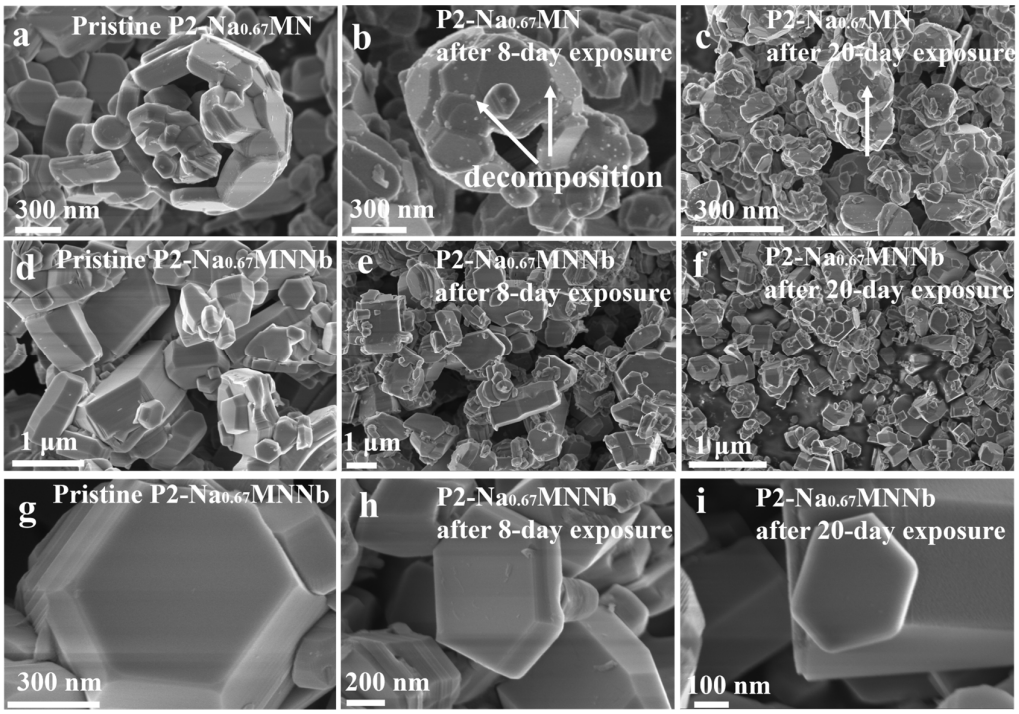

Figure 3. The SEM images of (**a**) pristine P2-$Na_{0.67}$MN and (**b**,**c**) P2-$Na_{0.67}$MN samples exposed in RH93% humid environment after different days of exposure. The SEM images of (**d**,**g**) pristine P2-$Na_{0.67}$MNNb. (**e**,**h**) P2-$Na_{0.67}$MNNb samples exposed in RH93% humid environment after 8 days of exposure. (**f**,**i**) P2-$Na_{0.67}$MNNb samples exposed in RH93% humid environment after 20 days of exposure.

Water molecules are important factors affecting the air stability of layered oxides. The insertion of water molecules led to an increase in layer spacing, the collapse of the Na_xTMO_2 structure and a decrease in electrochemical performance. So far, many studies have shown that CO_2 molecules in the air react with Na_xTMO_2, negatively affecting its morphology, crystal structure and electrochemical properties. Therefore, the mechanism of action between them on layered oxides is a topic worth discussing, and no unified conclusion has been reached at present. In this study, P2-$Na_{0.67}$MN and P2-$Na_{0.67}$MNNb were used as samples. As shown in Figures S4 and S5, the scanning electron microscope images of P2-$Na_{0.67}$MN and P2-$Na_{0.67}$MNNb were placed in the air for 20 days. However, the SEM image of P2-$Na_{0.67}$MN showed massive particles mixed with a large number of rod-like particles (indicated by orange ovals and arrows). The diameter of the rod-like particles ranged from 1.01 to 2.19 μm. Obviously, the rod-like particles were not P2-$Na_{0.67}$MN samples. In order to explore the composition of the rod-like particles, the element mapping of Na, O, Ni and Mn in P2-$Na_{0.67}$MN was demonstrated in Figures S6 and S7. Obviously, the rod-like particles did not contain Ni and Mn; Na and O uniformly dispersed in the selected region of the EDS. Infrared spectra showed CO_2^{3-} bands at 1620 cm^{-1} and 1128 cm^{-1}, and O-H bands at 3462 cm^{-1} (Figure S8). According to the FTIR and EDS mapping results, $NaHCO_3$ was clearly identified. The presence of CO_2 greatly influenced the structural transformation of P2-Na_xTMO_2 under ambient air exposure. Water molecules would insert into the Na layer or exchange Na^+ with H^+, leading to the expansion of the layer spacing and the formation of impurity phase. For most of the layered metal oxides in Na_xTMO_2, water molecules can release H^+ in exchange for Na^+ and maintain charge conservation through the loss of Na^+, which is the Na^+/H^+ exchange reaction. In addition, the CO_3^{2-} generated by the reaction of H_2O and CO_2 in moist air will enter the tetrahedral gap of the

transition metal layer, and the CO_3^{2-} will form the impurity $NaHCO_3$ with H^+ and Na^+. This process can be represented by the following formula:

$$xCO_2 + xH_2O + Na_yMO_2 = Na_{y-x}H_xMO_2 + xNaHCO_3$$

Compared with P2-$Na_{0.67}$MN, the SEM images of P2-$Na_{0.67}$MNNb showed no large number of rod-like particles, indicating that the doping of high-valence niobium enhanced the stability of the transition metal layer and had a certain shielding effect on water and carbon dioxide. The doping of niobium was effective for improving the air stability.

To further explain the outstanding air stability of P2-$Na_{0.67}$MNNb, high-resolution TEM imaging, electron diffraction techniques and HAADF-EDS mapping were used. As depicted in Figure 4a–e, the HRTEM and the magnification images of P2-$Na_{0.67}$MNNb showed clear stripes and high crystallinity. Interestingly, it was observed that the lattice arrangement of the P2-$Na_{0.67}$MNNb surface region was different from that of the bulk phase, which indicated that Nb doping led to changes in the material surface layer, forming a surface preconstructed layer (Figure 4c). The lattice spacing of the bulk phase was 0.557 nm, corresponding to (002) crystal plane of P2 structure, and the lattice spacing of the surface phase was 0.269 nm, which confirmed the existence of a phase interface between the bulk and the surface (Figure 4d,e). The thickness of the surface preconstructed layer (yellow arrow) was 3.282 nm. The hexagonal layered structure of the P2 structure was then determined by the selected area electron diffraction (SAED) pattern (Figure 4f). The TEM images of P2-$Na_{0.67}$MN showed that the lattice spacing was 0.556 nm, corresponding to the (002) crystal plane of the P2 structure (Figure S9). The HAADF-EDS mapping was used to further explore the element distribution of P2-$Na_{0.67}$MNNb from the bulk phase to the surface phase (Figure 4g and Figure S10). It was found that Na concentration in the surface preconstructed layer was relatively low, but Nb concentration in the same region was relatively high, indicating that Nb^{5+} tended to replace Na^+ on the surface. These results indicated that a Nb^{5+} rich preconstructed layer (3~5 nm, cation-mixed layer) was formed when Nb was doped into P2-$Na_{0.67}$MN. The pre-constructed layered structure effectively prevented the Na^+/H^+ exchange reaction, effectively resisted the entry of water molecules into the lattice and significantly improved the air stability of P2-$Na_{0.67}$MN [6].

In this part, P2-$Na_{0.67}$MNNb and P2-$Na_{0.67}$MN were used as samples to study how exposure to a humid environment affected the electrochemical performance of batteries. P2-$Na_{0.67}$MNNb and P2-$Na_{0.67}$MN under two conditions (1. exposed to RH93% moisture for 20 days and 2. in the pristine state) were assembled with Na metals. Figure 5a–h displays the electrochemical performance of fresh electrodes and those exposed to RH93% moisture for 20 days. Figure 5a,b displays the charge–discharge curves of pristine P2-$Na_{0.67}$MNNb and P2-$Na_{0.67}$MNNb exposed to RH93% moisture for 20 days at 0.2 C (1 C = 180 mAh g^{-1}) during the first three cycles. For the pristine P2-$Na_{0.67}$MNNb cathode material, two platforms appear above 3.0 V, corresponding to the redox reaction of $Ni^{2+}/Ni^{3+}/Ni^{4+}$. However, in the first three cyclic charge–discharge curves of the exposed P2-$Na_{0.67}$MNNb, in addition to the platform provided by the transition metal, there were some small voltage drops in the 2.0 V to 2.5 V voltage range, caused by the Na^+/vacancy ordering (Figure 5b). The redox potential of P2-$Na_{0.67}$MNNb before and after exposure was very similar and the discharge capacity was not significantly different. Figure 5c showed the rate performance of pristine P2-$Na_{0.67}$MNNb and exposed P2-$Na_{0.67}$MNNb. Pristine P2-$Na_{0.67}$MNNb displayed the reversible discharge capacities of 82.6, 81.7, 81.2, 80.3, 78, 76 and 76 mAh g^{-1} at 0.2, 0.5, 1, 2, 5, 10 and 20 C, respectively. The reversible discharge capacities of exposed P2-$Na_{0.67}$MNNb at 0.2, 0.5, 1, 2, 5, 10 and 20 C were 84.1, 84.1, 82.4, 81.4, 78.4, 75.6 and 72.5 mAh g^{-1}, respectively, showing no significant difference. The charge–discharge curves of the first three cycles before and after exposure to P2-$Na_{0.67}$MN were displayed in Figure S11. The charge and discharge curves of the first three cycles of P2-$Na_{0.67}$MN before and after exposure were similar, but P2-$Na_{0.67}$MN showed abnormal discharge capacity after exposure [46]. Figure 5d was the rate performance of P2-$Na_{0.67}$MN before and after exposure. As can be seen from Figure 5d, abnormal electrochemical phenomena were also

observed in P2-$Na_{0.67}$MN after exposure, such as very low coulomb efficiency (72% on average), further confirming the loss of Na^+ ions during exposure. Figure 5e,f shows the charge–discharge curves of pristine P2-$Na_{0.67}$MN and exposed P2-$Na_{0.67}$MN at different rates. It was clearly observed that the specific discharge capacity of exposed P2-$Na_{0.67}$MN was much smaller than the specific charge capacity, and the coulomb efficiency was low.

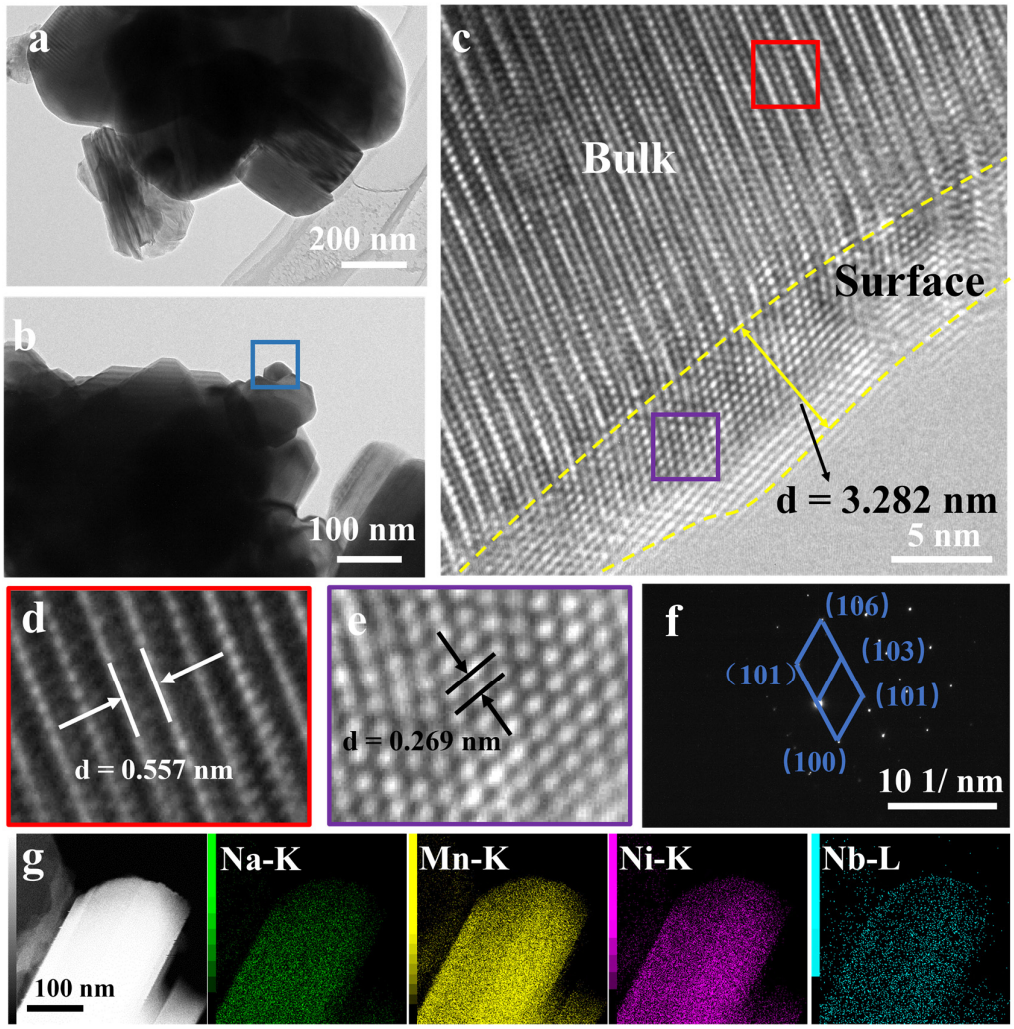

Figure 4. (**a**,**b**) The TEM and (**c**) the HRTEM of P2-$Na_{0.67}$MNNb. Enlarged images of the (**d**) red and (**e**) purple boxes in (**c**). (**f**) SAED pattern of P2-$Na_{0.67}$MNNb (the SAED pattern was selected from the blue box in (**b**)). (**g**) HAADF-EDS elemental mappings of P2-$Na_{0.67}$MNNb (including Na-K edge, Mn-K edge, Ni-K edge and Nb-L edge).

The capacity retention of pristine P2-$Na_{0.67}$MNNb and exposed P2-$Na_{0.67}$MNNb were 84.64% and 84.43%, respectively, during 1000 cycles in 5 C, with no significant change (Figure 5g). Conversely, P2-$Na_{0.67}$MN showed severe capacity loss at 5 C and discharge capacity retention of 80.32% for pristine $Na_{0.67}$MN and 56.33% for exposed $Na_{0.67}$MN after 1000 cycles. It was evident that the exposed P2-$Na_{0.67}$MN significantly reduced the discharge capacity, the coulomb efficiency and capacity retention rate. The electrochemical performance of P2-$Na_{0.67}$MN was more obviously reduced after exposure than that of P2-$Na_{0.67}$MNNb, which showed that P2-$Na_{0.67}$MNNb had better air and electrochemical stabilities. Electrochemical impedance spectroscopy (EIS) was employed to identify the resistance of the battery. The resistance of the battery that based on P2-$Na_{0.67}$MNNb before and after exposure was 280 Ω and 300 Ω, respectively, and that of P2-$Na_{0.67}$MN before and after exposure was 300 Ω and 380 Ω, respectively (Figure S12). The charge transfer resistance of the battery that based on pristine P2-$Na_{0.67}$MN and exposed P2-$Na_{0.67}$MN after

1000 cycles at 5 C was 906 Ω and 2049 Ω, respectively, and that of pristine P2-$Na_{0.67}$MNNb and exposed P2-$Na_{0.67}$MNNb was 380 Ω and 619 Ω, respectively (Figure 5h). These results indicated that Nb doping effectively reduced the charge transfer resistance of sodium ion intercalation/de-intercalation. Even after moist air exposure or 1000 cycles of charge and discharge, the charge transfer resistance of the P2-$Na_{0.67}$MNNb based battery was much smaller than P2-$Na_{0.67}$MN. Compared with P2-$Na_{0.67}$MN, P2-$Na_{0.67}$MNNb exhibited excellent water resistance and electrochemical stability.

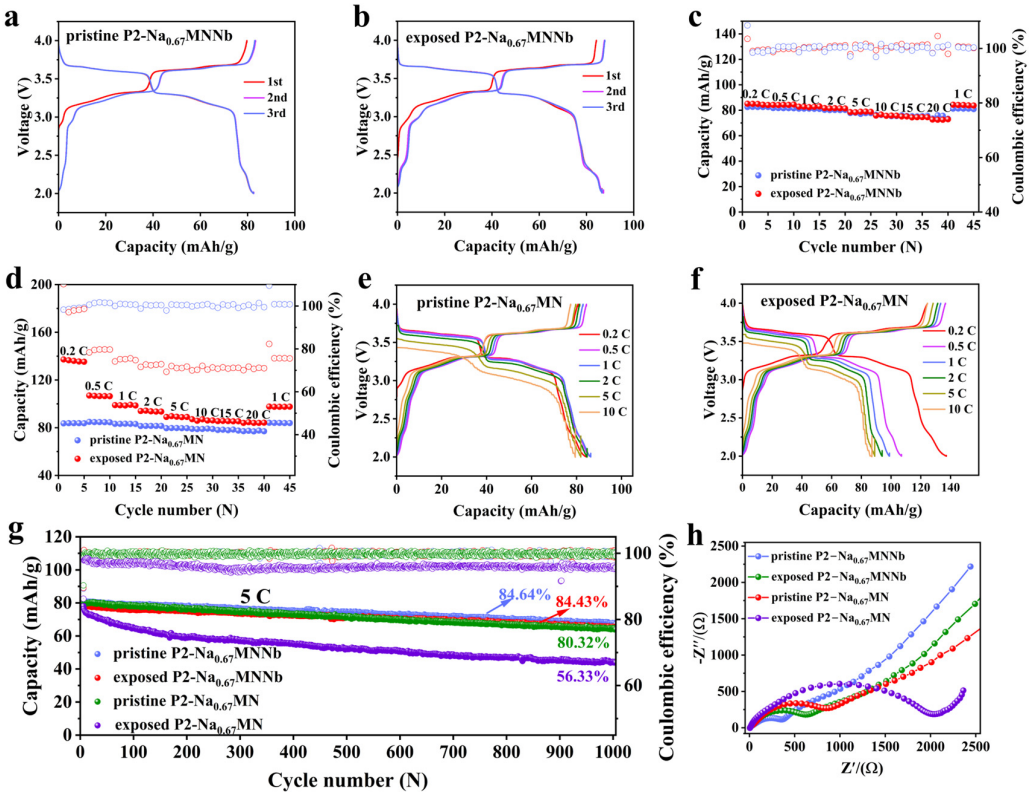

Figure 5. (**a**,**b**) Galvanostatic charge/discharge voltage profiles of the pristine P2-$Na_{0.67}$MNNb and exposed P2-$Na_{0.67}$MNNb at the first three cycles in the voltage range of 2–4 V, respectively (exposed P2-$Na_{0.67}$MNNb refers to exposing pristine P2-$Na_{0.67}$MNNb to RH93% humid environment for 20 days). (**c**) Rate capability of pristine P2-$Na_{0.67}$MNNb and exposed P2-$Na_{0.67}$MNNb. (**d**) Rate capability of pristine P2-$Na_{0.67}$MN and exposed P2-$Na_{0.67}$MN. Charge and discharge curves of (**e**) pristine P2-$Na_{0.67}$MN and (**f**) exposed P2-$Na_{0.67}$MN at different current densities. (**g**) Electrochemical cycling performance of pristine P2-$Na_{0.67}$MN, exposed P2-$Na_{0.67}$MN, pristine P2-$Na_{0.67}$MNNb and exposed P2-$Na_{0.67}$MNNb at a rate of 5 C for 1000 cycles. (**h**) Nyquist plot of the coin cells that based on pristine P2-$Na_{0.67}$MN, exposed P2-$Na_{0.67}$MN, pristine P2-$Na_{0.67}$MNNb and exposed P2-$Na_{0.67}$MNNb electrode materials after 1000 cycles at a rate of 5 C.

To further explore the mechanism of the excellent electrochemical performance of P2-$Na_{0.67}$MNNb and the influence of the surface preconstructed layer, the microstructure change after 500 cycles was also studied by HRTEM. The HRTEM results showed that the thickness of the P2-$Na_{0.67}$MNNb surface layer remained at 3~5 nm after 500 cycles, the bulk structure remained basically unchanged and the lattice spacing was 0.559 nm (Figure 6a). After 500 cycles, about 2~3 nm CEI (cathode–electrolyte interphase) was formed on the P2-$Na_{0.67}$MNNb cathode surface. The thin and stable CEI layer not only reduced charge transfer resistance but also benefited electrochemical stability. In contrast, with P2-$Na_{0.67}$MN there was serious surface degradation and the thickness of CEI was 9.83 nm (Figure 6b). These results indicated that Nb rich preconstructed layer played a role in inhibiting the surface degradation of P2 material during the electrochemical reaction

and forming a stable and thin CEI layer, thus reducing the charge transfer resistance and preventing water molecules from entering the lattice.

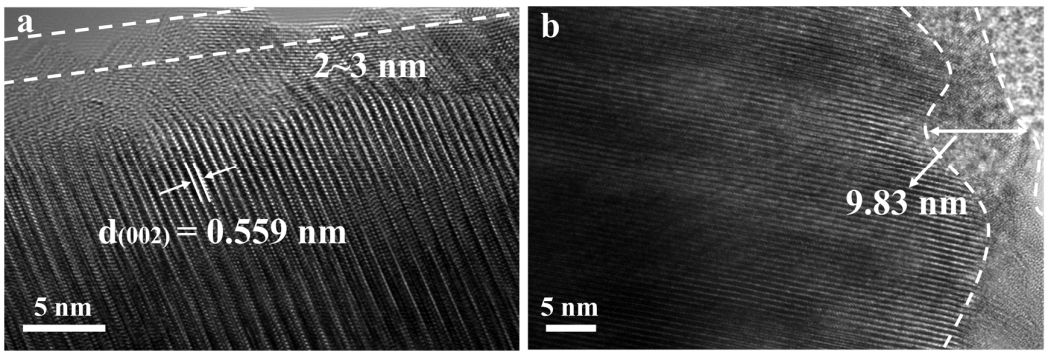

Figure 6. The HRTEM images of (**a**) P2-$Na_{0.67}$MNNb and (**b**) P2-$Na_{0.67}$MN after 500 cycles at 1 C and 25 °C in coin cells.

4. Conclusions

In this paper, P2-$Na_{0.67}$MN and P2-$Na_{0.67}$MNNb were successfully prepared, and the air stability of these materials in different environments were comprehensively studied. Nb doping greatly improved the air and electrochemical stabilities of P2-$Na_{0.67}$MN. We successfully increased the c-axis spacing of P2-$Na_{0.67}$MN after Nb^{5+} doping and introduced the Nb-O bond with strong bond energy (753 kJ mol^{-1}), which improved the structure stability of the transition metal layer. In addition, the Nb-doping induced surface pre-constructed layer played an important role in stopping the surface degradation of the P2 material during the electrochemical reaction, forming a stable and thin CEI film, reducing the charge transfer resistance and preventing the entry of water molecules into the lattice of the material. Nb doping significantly promoted cycling stability, air stability and the rate performance of P2-$Na_{0.67}$MN, resulting in a better sodium storage property. P2-$Na_{0.67}$MNNb exhibited superior rate performance (a reversible capacity of 72.5 mAh g^{-1} at 20 C) and outstanding cycling performance (84.43% capacity retention after 1000 cycles at 5 C) in a half cell after being exposed in a moisture atmosphere (RH93%) for 20 days. This work has provided a new strategy for improving the air stability of layered oxide materials for sodium-ion batteries.

Supplementary Materials: The following supporting information can be downloaded at: https://www.mdpi.com/article/10.3390/batteries9030183/s1, Figure S1: (a) The precursor SEM of P2-Na0.67MN and P2-Na0.67MNNb. (b) The precursor SEM of P2-Na0.67MN and P2-Na0.67MNNb.; Figure S2: The XRD patterns of P2-Na0.67Mn0.67Ni0.33Nb0.05O2; Figure S3: (a) The XRD patterns of P2-Na0.67MNNb sample exposed in different atmosphere after 20-day exposure. (b) The XRD patterns of water-immersed P2-Na0.67MNNb sample; Figure S4: (a) The SEM of P2-Na0.67MN after 20 days of air exposure. (b) The SEM of P2-Na0.67MN after 20 days of air exposure; Figure S5: The SEM of P2-Na0.67MNNb after 20 days of air exposure; Figure S6: SEM-EDS elemental mappings of rod-like particles in P2-Na0.67MN sample; Figure S7: The spectrum diagram of total distribution diagram for SEM-EDS of rod-like particles in P2-Na0.67MN sample; Figure S8: The FTIR of P2-Na0.67MN after 20 days of air exposure; Figure S9: (a) The TEM images of P2-Na0.67MN. (b) The TEM images of P2-Na0.67MN; Figure S10: The spectrum diagram of total distribution diagram for HADDF-EDS of P2-Na0.67MNNb; Figure S11: Galvanostatic charge/discharge voltage profiles of (a) the pristine P2-Na0.67MN and (b) exposed P2-Na0.67MN at the first three cycles at 0.2 C in the voltage range of 2-4 V (exposed P2-Na0.67MN refers to exposing pristine P2-Na0.67MN to RH93% humid environment for 20 days); Figure S12: Nyquist plot of the coin cells that based on pristine P2-Na0.67MN, exposed P2-Na0.67MN, pristine P2-Na0.67MNNb and exposed P2-Na0.67MNNb electrode materials; Table S1: The ICP date of P2-Na0.67MN and P2-Na0.67MNNb cathode materials; Table S2: Crystallographic parameters of P2-Na0.67MNNb refined by the Rietveld method; Table S3: Crystallographic parameters of P2-Na0.67MN refined by the Rietveld method.

Author Contributions: Y.Z., Z.W. and W.F. designed and guided the work. Y.C. and Q.S. performed the experiments. Y.C. wrote the paper with support from Q.S., S.Z., Y.L. and X.Y. All authors have read and agreed to the published version of the manuscript.

Funding: The research was funded by the National Natural Science Foundation of China (22179077), Shanghai Science and Technology Commission's "2020 Science and Technology In-novation Action Plan" (20511104003), Natural Science Foundation in Shanghai (21ZR1424200), Hebei Natural Science Foundation for Distinguished Young Scholars (B2017203313), and the Scientific Research Foundation for the Returned Overseas Chinese Scholars (CG2014003002).

Data Availability Statement: The data that support the findings of this study are available from the corresponding author upon reasonable request.

Conflicts of Interest: The authors declare no conflict of interest.

References

1. Zuo, W.; Xiao, Z.; Zarrabeitia, M.; Xue, X.; Yang, Y.; Passerini, S. Guidelines for Air-Stable Lithium/Sodium Layered Oxide Cathodes. *ACS Mater. Lett.* **2022**, *4*, 1074–1086. [CrossRef]
2. Zhang, R.; Yang, S.; Li, H.; Zhai, T.; Li, H. Air sensitivity of electrode materials in Li/Na ion batteries: Issues and strategies. *InfoMat* **2022**, *4*, e12305. [CrossRef]
3. Yao, H.-R.; Zheng, L.; Xin, S.; Guo, Y.-G. Air-stability of sodium-based layered-oxide cathode materials. *Sci. China Chem.* **2022**, *65*, 1076–1087. [CrossRef]
4. Chen, T.R.; Sheng, T.; Wu, Z.G.; Li, J.T.; Wang, E.H.; Wu, C.J.; Li, H.T.; Guo, X.D.; Zhong, B.H.; Huang, L.; et al. Cu(2+) Dual-Doped Layer-Tunnel Hybrid Na(0.6)Mn(1−x)Cu (x)O(2) as a Cathode of Sodium-Ion Battery with Enhanced Structure Stability, Electrochemical Property, and Air Stability. *ACS Appl. Mater Interfaces* **2018**, *10*, 10147–10156. [CrossRef]
5. Boyd, S.; Augustyn, V. Transition metal oxides for aqueous sodium-ion electrochemical energy storage. *Inorg. Chem. Front.* **2018**, *5*, 999–1015. [CrossRef]
6. Guo, S.; Li, Q.; Liu, P.; Chen, M.; Zhou, H. Environmentally stable interface of layered oxide cathodes for sodium-ion batteries. *Nat. Commun.* **2017**, *8*, 135. [CrossRef]
7. Xu, C.; Cai, H.; Chen, Q.; Kong, X.; Pan, H.; Hu, Y.-S. Origin of Air-Stability for Transition Metal Oxide Cathodes in Sodium-Ion Batteries. *ACS Appl. Mater. Interfaces* **2022**, *14*, 5338–5345. [CrossRef]
8. Buchholz, D.; Chagas, L.G.; Vaalma, C.; Wu, L.; Passerini, S. Water sensitivity of layered P2/P3-NaxNi0.22Co0.11Mn0.66O2 cathode material. *J. Mater. Chem. A* **2014**, *2*, 13415–13421. [CrossRef]
9. Zuo, W.; Liu, X.; Qiu, J.; Zhang, D.; Xiao, Z.; Xie, J.; Ren, F.; Wang, J.; Li, Y.; Ortiz, G.F.; et al. Engineering Na(+)-layer spacings to stabilize Mn-based layered cathodes for sodium-ion batteries. *Nat. Commun.* **2021**, *12*, 4903. [CrossRef]
10. Zheng, L.; Li, J.; Obrovac, M.N. Crystal Structures and Electrochemical Performance of Air-Stable Na2/3Ni1/3–xCuxMn2/3O2 in Sodium Cells. *Chem. Mater.* **2017**, *29*, 1623–1631. [CrossRef]
11. Whittingham, M.S. Ultimate Limits to Intercalation Reactions for Lithium Batteries. *Chem. Rev.* **2014**, *114*, 11414–11443. [CrossRef] [PubMed]
12. Zuo, W.; Qiu, J.; Liu, X.; Zheng, B.; Zhao, Y.; Li, J.; He, H.; Zhou, K.; Xiao, Z.; Li, Q.; et al. Highly-stable P2–Na0.67MnO2 electrode enabled by lattice tailoring and surface engineering. *Energy Storage Mater.* **2019**, *26*, 503–512. [CrossRef]
13. Zhang, Y.; Zhang, R.; Huang, Y. Air-Stable Na (x) TMO(2) Cathodes for Sodium Storage. *Front. Chem.* **2019**, *7*, 335. [CrossRef]
14. Wang, P.-F.; You, Y.; Yin, Y.-X.; Guo, Y.-G. Layered Oxide Cathodes for Sodium-Ion Batteries: Phase Transition, Air Stability, and Performance. *Adv. Energy Mater.* **2018**, *8*, 1701912. [CrossRef]
15. Boyd, S.; Dhall, R.; LeBeau, J.M.; Augustyn, V. Charge storage mechanism and degradation of P2-type sodium transition metal oxides in aqueous electrolytes. *J. Mater. Chem. A* **2018**, *6*, 22266–22276. [CrossRef]
16. Yabuuchi, N.; Kubota, K.; Dahbi, M.; Komaba, S. Research Development on Sodium-Ion Batteries. *Chem. Rev.* **2014**, *114*, 11636–11682. [CrossRef] [PubMed]
17. You, Y.; Dolocan, A.; Li, W.; Manthiram, A. Understanding the Air-Exposure Degradation Chemistry at a Nanoscale of Layered Oxide Cathodes for Sodium-Ion Batteries. *Nano Lett.* **2019**, *19*, 182–188. [CrossRef]
18. Han, M.H.; Sharma, N.; Gonzalo, E.; Pramudita, J.C.; Brand, H.E.A.; del Amo, J.M.L.; Rojo, T. Moisture exposed layered oxide electrodes as Na-ion battery cathodes. *J. Mater. Chem. A* **2016**, *4*, 18963–18975. [CrossRef]
19. Duffort, V.; Talaie, E.; Black, R.; Nazar, L.F. Uptake of CO_2 in Layered P2-Na0.67Mn0.5Fe0.5O2: Insertion of Carbonate Anions. *Chem. Mater.* **2015**, *27*, 2515–2524. [CrossRef]
20. Pritzl, D.; Teufl, T.; Freiberg, A.T.S.; Strehle, B.; Sicklinger, J.; Sommer, H.; Hartmann, P.; Gasteiger, H.A. Editors' Choice—Washing of Nickel-Rich Cathode Materials for Lithium-Ion Batteries: Towards a Mechanistic Understanding. *J. Electrochem. Soc.* **2019**, *166*, A4056–A4066. [CrossRef]

21. Grey, C.P.; Tarascon, J.M. Sustainability and in situ monitoring in battery development. *Nat. Mater.* **2016**, *16*, 45–56. [CrossRef]
22. Kim, H.; Hong, J.; Park, K.-Y.; Kim, H.; Kim, S.-W.; Kang, K. Aqueous Rechargeable Li and Na Ion Batteries. *Chem. Rev.* **2014**, *114*, 11788–11827. [CrossRef] [PubMed]
23. Li, Y.; Feng, X.; Cui, S.; Shi, Q.; Mi, L.; Chen, W. From α-NaMnO2to crystal water containing Na-birnessite: Enhanced cycling stability for sodium-ion batteries. *Cryst. Eng. Comm.* **2016**, *18*, 3136–3141. [CrossRef]
24. Delmas, C.; Fouassier, C.; Hagenmuller, P. Structural classification and properties of the layered oxides. *Phys. B+C* **1980**, *99*, 81–85. [CrossRef]
25. You, Y.; Song, B.; Jarvis, K.; Huq, A.; Manthiram, A. Insights into the Improved Chemical Stability against Water of LiF-Incorporated Layered Oxide Cathodes for Sodium-Ion Batteries. *ACS Mater. Lett.* **2019**, *1*, 89–95. [CrossRef]
26. Liang, X.; Sun, Y.-K. A Novel Pentanary Metal Oxide Cathode with P2/O3 Biphasic Structure for High-Performance Sodium-Ion Batteries. *Adv. Funct. Mater.* **2022**, *32*, 2206154. [CrossRef]
27. Wang, J.E.; Kim, H.; Jung, Y.H.; Kim, D.K.; Kim, D.J. Designing High Energy Sodium-Ion Battery Cathodes by Utilizing P2/O3 Biphasic Structure and Lithium Honeycomb Ordering. *Small* **2021**, *17*, 2100146. [CrossRef]
28. Zhou, Y.-N.; Wang, P.-F.; Zhang, X.-D.; Huang, L.-B.; Wang, W.-P.; Yin, Y.-X.; Xu, S.; Guo, Y.-G. Air-Stable and High-Voltage Layered P3-Type Cathode for Sodium-Ion Full Battery. *ACS Appl. Mater. Interfaces* **2019**, *11*, 24184–24191. [CrossRef]
29. Zheng, Y.-M.; Huang, X.-B.; Meng, X.-M.; Xu, S.-D.; Chen, L.; Liu, S.-B.; Zhang, D. Copper and Zirconium Codoped O3-Type Sodium Iron and Manganese Oxide as the Cobalt/Nickel-Free High-Capacity and Air-Stable Cathode for Sodium-Ion Batteries. *ACS Appl. Mater. Interfaces* **2021**, *13*, 45528–45537. [CrossRef]
30. Qi, R.; Chu, M.; Zhao, W.; Chen, Z.; Liao, L.; Zheng, S.; Chen, X.; Xie, L.; Liu, T.; Ren, Y.; et al. A highly-stable layered Fe/Mn-based cathode with ultralow strain for advanced sodium-ion batteries. *Nano Energy* **2021**, *88*, 106206. [CrossRef]
31. Zhou, P.; Che, Z.; Ma, F.; Zhang, J.; Weng, J.; Wu, X.; Miao, Z.; Lin, H.; Zhou, J.; Zhuo, S. Designing water/air-stable P2-layered cathodes with delayed P2–O2 phase transition by composition and structure engineering for sodium-ion batteries at high voltage. *Chem. Eng. J.* **2021**, *420*, 127667. [CrossRef]
32. Jiang, J.; He, H.-C.; Cheng, C.; Yan, T.; Xia, X.; Ding, M.; He, L.; Chan, T.-S.; Zhang, L. Improving Structural and Moisture Stability of P2-Layered Cathode Materials for Sodium-Ion Batteries. *ACS Appl. Energy Mater.* **2022**, *5*, 1252–1261. [CrossRef]
33. Li, X.; Shen, X.; Zhao, J.; Yang, Y.; Zhang, Q.; Ding, F.; Han, M.; Xu, C.; Yang, C.; Liu, H.; et al. O3-NaFe(1/3–x)Ni1/3Mn1/3AlxO2 Cathodes with Improved Air Stability for Na-Ion Batteries. *ACS Appl. Mater. Interfaces* **2021**, *1*, 33015–33023. [CrossRef] [PubMed]
34. Lu, Z.; Dahn, J.R. Intercalation of Water in P2, T2 and O2 Structure Az[CoxNi1/3-xMn2/3]O2. *Chem. Mater.* **2001**, *13*, 1252–1257. [CrossRef]
35. Wang, X.; Yin, X.; Feng, X.; Li, Y.; Dong, X.; Shi, Q.; Zhao, Y.; Zhang, J. Rational Design of Na0.67Ni0.2Co0.2Mn0.6O2 Microsphere Cathode Material for Stable and Low Temperature Sodium Ion Storage. *Chem. Eng. J.* **2022**, *428*, 130990. [CrossRef]
36. Yao, H.-R.; Wang, P.-F.; Gong, Y.; Zhang, J.; Yu, X.; Gu, L.; OuYang, C.; Yin, Y.-X.; Hu, E.; Yang, X.-Q.; et al. Designing Air-Stable O3-Type Cathode Materials by Combined Structure Modulation for Na-Ion Batteries. *J. Am. Chem. Soc.* **2017**, *139*, 8440–8443. [CrossRef]
37. Kubota, K.; Komaba, S. Review—Practical Issues and Future Perspective for Na-Ion Batteries. *J. Electrochem. Soc.* **2015**, *162*, A2538–A2550. [CrossRef]
38. Zuo, W.; Qiu, J.; Liu, X.; Ren, F.; Liu, H.; He, H.; Luo, C.; Li, J.; Ortiz, G.F.; Duan, H.; et al. The stability of P2-layered sodium transition metal oxides in ambient atmospheres. *Nat. Commun.* **2020**, *11*, 3544. [CrossRef]
39. Wang, X.; Dong, X.; Feng, X.; Shi, Q.; Wang, J.; Yin, X.; Zhang, J.; Zhao, Y. In-Plane BO_3 Configuration in P2 Layered Oxide Enables Outstanding Long Cycle Performance for Sodium Ion Batteries. *Small Methods* **2023**, *7*, 2201201. [CrossRef] [PubMed]
40. Nam, K.W.; Kim, S.; Yang, E.; Jung, Y.; Levi, E.; Aurbach, D.; Choi, J.W. Critical Role of Crystal Water for a Layered Cathode Material in Sodium Ion Batteries. *Chem. Mater.* **2015**, *27*, 3721–3725. [CrossRef]
41. Chu, S.; Jia, X.; Wang, J.; Liao, K.; Zhou, W.; Wang, Y.; Shao, Z. Reduced air sensitivity and improved electrochemical stability of P2–Na2/3Mn1/2Fe1/4Co1/4O2 through atomic layer deposition-assisted Al_2O_3 coating. *Compos. Part B* **2019**, *173*, 106913. [CrossRef]
42. Wang, Y.; Tang, K.; Li, X.; Yu, R.; Zhang, X.; Huang, Y.; Chen, G.; Jamil, S.; Cao, S.; Xie, X.; et al. Improved cycle and air stability of P3-Na0.65Mn0.75Ni0.25O2 electrode for sodium-ion batteries coated with metal phosphates. *Chem. Eng. J.* **2019**, *372*, 1066–1076. [CrossRef]
43. Lamb, J.; Manthiram, A. Surface-Modified Na(Ni0.3Fe0.4Mn0.3)O2 Cathodes with Enhanced Cycle Life and Air Stability for Sodium-Ion Batteries. *ACS Appl. Energy Mater.* **2021**, *4*, 11735–11742. [CrossRef]
44. Zheng, L.; Li, L.; Shunmugasundaram, R.; Obrovac, M.N. Effect of Controlled-Atmosphere Storage and Ethanol Rinsing on NaNi0.5Mn0.5O2 for Sodium-Ion Batteries. *ACS Appl. Mater. Interfaces* **2018**, *10*, 38246–38254. [CrossRef]
45. Zhang, J.; Yu, D.Y. Stabilizing Na0.7MnO2 cathode for Na-ion battery via a single-step surface coating and doping process. *J. Power Sources* **2018**, *391*, 106–112. [CrossRef]

46. Feng, X.; Li, Y.; Shi, Q.; Wang, X.; Yin, X.; Wang, J.; Xia, Z.; Xiao, H.; Chen, A.; Yang, X.; et al. A comprehensive modification enables the high rate capability of P2-Na0.75Mn0.67Ni0.33O2 for sodium-ion cathode materials. *J. Energy Chem.* **2022**, *69*, 442–449. [CrossRef]
47. Shi, Q.; Qi, R.; Feng, X.; Wang, J.; Li, Y.; Yao, Z.; Wang, X.; Li, Q.; Lu, X.; Zhang, J.; et al. Niobium-doped layered cathode material for high-power and low-temperature sodium-ion batteries. *Nat. Commun.* **2022**, *13*, 3205. [CrossRef]